Laser ultrasonic wave spatial gradient features for damage detection

Zihan WU[a] and Michael D. TODD[b*]

Dept. of Structural Engineering, University of California San Diego, 9500 Gilman Drive 0085,
La Jolla, CA 92093-0085 USA

[a]z5wu@eng.ucsd.edu, [b]mdtodd@eng.ucsd.edu

Keywords: Laser Ultrasonics, Spatial Gradient, Covariance, Ultrasonic Imaging

Abstract. This work presents a damage imaging method exploiting full-field guided ultrasonic waves excited by a thermoelastic-effect laser. From the high spatial resolution data produced, a spatial gradient–based image processing technique was developed using gradient vectors to extract features sensitive to defects. Localized mechanical impedance changes in the damaged area induce a local distortion of the waveform, which was quantified by the variation of the gradient vectors in the scanning area as time evolves. Such variation was accumulated over time with an analytically derived optimal statistical threshold filter to generate a gradient-orientation map for damage imaging. The proposed algorithm is shown to detect distinctive damage patterns when tested experimentally on a 3 mm aluminum plate with multiple simultaneous simulated defects. Compared to conventional techniques like local wavenumber estimation, the generation of the accumulated orientation map involves no filtering process in the frequency or wavenumber domain, but it comes at the expense of less accurate shaping of the defect. A spatial covariance analysis was adopted to locate damage from the results as well as to evaluate the correlation among different kinds of defects.

Introduction

Ultrasonic guided waves are a very common technique used for defect detection and localization in plate-like structures due to their propagation coverage and scattering sensitivity to such defects [1-3]. Various architectures to excite and detect ultrasonic waves have been implemented, and more recently, laser ultrasonic methods have evolved as a powerful approach because full-field (spatio-temporally dense) interrogation and imaging are possible in relatively rapid inspection timeframes by taking advantage of reciprocity assumptions. The resulting rich information field (space-time-frequency) may be processed in several ways to achieve defect detection/localization, including various multi-dimensional Fourier analysis, wavelet or other time-frequency analysis, compressed sensing, matched filtering, optimization strategies, and others [4-12].

Beyond these approaches applied to high-resolution laser ultrasonic data, the potential of employing spatial gradient analyses in these imaged data sets has only been recently explored [13]. In the image recognition field, spatio-temporal gradient orientation correlation metrics may be used to recognize a moving object in video data [14]. In the present application space, the hypothesis becomes that defect scatterers may be reflected changes in spatial gradient field as time progresses. This work reports on the use of gradient vectors at each point to indicate local waveform distortions presumably induced by highly localized defect scatterers. The derivation of the proposed method involves no frequency tuning or wave mode decomposition, so it is computationally efficient and requires little manual oversight in practice. Additionally, the process removes the complex wave patterns of guided waves and visually enhances the distortion caused by the defects for more intuitive identification and interpretation. In this approach, the measured ultrasonic waveform imaged (UWI) data are stored in the angle-radius (φ-R) polar domain through a circle laser scanning pattern that allows the evaluation of spatial covariance analysis for fast detection. UWI data in the polar coordinate space can be converted to Cartesian coordinates for

more intuitive visualization and interpretation. First, the experimental setup to obtain the full-field ultrasonic wavefield data from the specimen with and without artificial defects is discussed, and then the spatial gradient analysis method applied to UWI data is presented. Finally, results and a summary are presented.

Experimental Architecture

Fig. 1(a) shows a schematic diagram of the laser ultrasonic interrogation system. This system consists of a laser scanning system incorporated with a signal conditioning device, a data acquisition (DAQ) module, a contact sensor, and a computer used for signal processing and operation control. The laser scanning system has a two-dimensional laser scanner and a diode-pumped solid-state Q-switched Nd:YAG laser. The Q-switched laser is composed of a laser controller and a laser head with an output beam of 527 nm wavelength and pulse repetition rates (PRR) from single-shot to 1 kHz. The 2D laser scanner is used to synchronize the 2-axis galvanometer scanner (Fig. 1(b)) with the Q-switched laser to maneuver the laser impinging point rapidly on a target at a PRR according to the preset scanning pattern coordinates. A circular scanning pattern was considered, and the ultrasonic waves were generated and obtained at each coordinate of (R,θ) in the polar coordinate space. The scanning radius ranges were set from 20 mm to 220 mm with an interval of 1 mm, and the angular interval was set to 0.78°.

During the scanning process, a laser pulse impinges at a scan point, and the corresponding ultrasound is generated at the local point based on the thermoelastic principle. The generated ultrasound is then signal-conditioned through a contact sensor and digitized in the DAQ module as shown in Fig. 1(a). In the DAQ module, the generated ultrasound is digitized synchronously with the PRR of the laser scanning system by receiving a triggering signal from the laser controller after the laser pulse is emitted. In the digitizing process, the ultrasound is sampled for K number of data points at sampling time interval T_s and stored in a computer. The digitizing process is repeated as the scanning process is performed. In this paper, the K was set to 2000 at the sampling interval of $T_s = 0.1$ μs. All digitized data are represented in the form of a three-dimensional r-θ-t tensor, indexed by radial direction (j=1...N), circumferential direction (k=1...M), and time (i=1...K), respectively, with N=201 and M=460 in this work; we thus denote the symbol $U_{j,k,i}$ to indicate pixel intensity at (radial, circumferential) location (j,k) at time point i from the polar scan. Standard polar transformations may be used to return data to the Cartesian domain as needed.

The test specimen was a 3 mm thick aluminum plate. Four damage locations were considered in this article and denoted as L1, L2, L3, and L4 as indicated in Fig. 1(b) by the yellow circles. Three different simulated defect classes were deployed as shown in Fig. 1(c). Defect D1 is a 400 mm^2 plasticine mass attached at the rear scanning surface, which acted as a damper to attenuate the waves in its path. Defect D2 is a metallic screw, and the screw tip was polished flat and bonded to the rear scanning surface with a 5 mm diameter circular contact area between the tip and plate. Defect D3 is a 260 mm^2 surface area aluminum strip of a feeler gage. During the bonding process, a 20-mm-width Teflon sheet was sandwiched between the surface of the plate and strip to simulate a disbond.

Three simulated damage cases with the defects (D1–D3) at specific locations (L1–L4) as shown were considered. First, a single damage case was conducted where each defect was set and tested individually at corresponding locations. After that, a multi-location damage case was considered with three pieces of plasticine set at locations L1, L2, and L4 simultaneously. To compare the inter-defect correlation with spatial covariance analysis, the plasticine at L1 was replaced by a metallic screw while keeping the rest of the conditions unchanged. Finally, a multi-class damage case was studied by including all the three types of defects located at L1, L2, and L3, respectively.
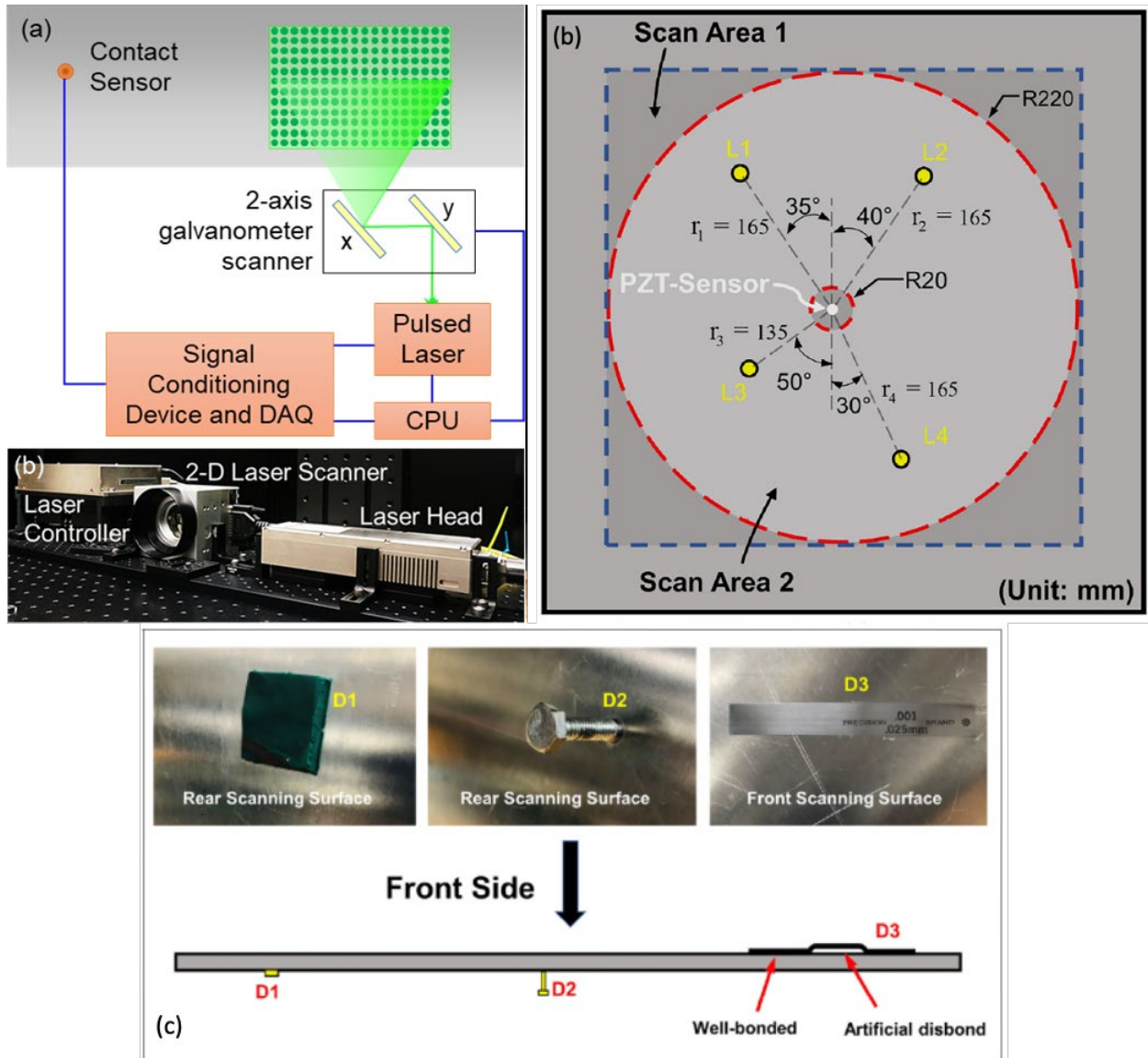
Fig. 1 (a) Laser ultrasonic interrogation system configuration, (b) 3 mm aluminum plate defect inspection configurations, and (c) detailed examples of the three defect classes. Figs. 1(b) and (c) were reproduced with permission from Ref. [13].

Spatial Gradient Analysis

Given any pixel measurement $U_{j,k,i}$, radial and circumferential gradients, $G^{(r)}_{j,k,i}$ and $G^{(\theta)}_{j,k,i}$, must be evaluated. To estimate the partial derivatives, a scale factor d that defines the neighborhood of pixels around the *j-k* location is needed; the size governs the usual trade-off between image spatial resolution (lower d) and signal-to-noise (higher d). Thus, we can use central differences to get the gradients directly, since are inherently collected in the polar domain, as in Eq. (1):

$$G^{(r)}_{j,k,i} = \frac{\partial U_{j,k,i}}{\partial r} = \frac{U_{j+d,k,i} - U_{j-d,k,i}}{2d}$$

$$G^{(\theta)}_{j,k,i} = \frac{\partial U_{j,k,i}}{\partial \theta} = \frac{U_{j,k+d,i} - U_{j,k-d,i}}{2d}$$

(1)

The two gradient vectors have a magnitude A and orientation phase angle P determined by

$$A_{j,k,i} = \sqrt{\left(G_{j,k,i}^{(r)}\right)^2 + \left(G_{j,k,i}^{(\theta)}\right)^2}$$
$$P_{j,k,i} = \tan^{-1}\left(G_{j,k,i}^{(\theta)} \big/ G_{j,k,i}^{(r)}\right) \tag{2}$$

The value of $d = 2$ was used in this work. The values of $A_{j,k,i}$ under the null hypothesis (no defects) were used as a statistically rigorous filter. Under the assumption of Gaussian pixel intensity noise with zero mean and standard deviation σ, and assuming nearest-neighbor pixel-to-pixel correlation to be ρ, it is readily shown [13] that the probability density of the gradient magnitudes is Rayleigh-distributed as

$$p\left(A_{j,k,i}\right) = \frac{2A_{j,k,i}d^2}{(1-\rho)\sigma^2} e^{-\frac{\left(A_{j,k,i}\right)^2 d^2}{(1-\rho)\sigma^2}} \tag{3}$$

Thus, by setting a confidence value α, Eq. (3) may be integrated from 0 up to a critical gradient magnitude threshold ε such that the integral equals α, resulting in $\varepsilon = \sqrt{(\rho-1)\log(1-\alpha)}\,(\sigma/d)$. Experiments on the defect-free specimens resulted in estimates of σ=0.04 and ρ=0.1. For a given α, only data for which $A_{j,k,i} > \varepsilon$ were retained. These statistically filtered datasets are denoted with prime marks, i.e., $A'_{j,k,i}$ and $P'_{j,k,i}$. The feature of interest going forward will be just the gradient orientation data, $P'_{j,k,i}$, as it is far more sensitive to local scattering effects than the magnitude of the gradient vector. The idea becomes that $P'_{j,k,i}$ will change in time as the wavefront encounters a defect; the magnitude of this orientation change would be given by

$$\Delta P'_{j,k,i} = \left| P'_{j,k,i+1} - P'_{j,k,i} \right| \tag{4}$$

It is natural to hypothesize that regions with different material properties or geometries may have significant gradient orientation variation compared to adjacent undamaged areas, i.e., the local area affected by the defect would have a larger *time-accumulated* variation in its gradient orientation, given by $F_{j,k}^{(test)} = \sum_{i=1}^{i_{max}} \Delta P'_{j,k,i}$, where i_{max} is the integration upper limit. This limit is the most "tweakable" parameter in this approach, as integrating too long brings in the complexity of reflected wave interactions and integrating too little doesn't accumulate maximal change in the feature. It was found that 60 μs provided a good balance. Baseline subtraction of the reference state is still employed in this case, resulting in a final test feature given by

$$F_{j,k} = F_{j,k}^{(test)} - F_{j,k}^{(baseline)} \tag{5}$$

A spatial orientation covariance method was introduced in [11] to localize the defects whereby a covariance matrix $C_{j,k}$ of the $F_{j,k}$ features was formed by averaging over columns (the radial direction) to find the orientation-to-orientation covariance structure. Thus, the angular orientation F_d of the damage location to the center of the plate was first determined by localizing the point with the largest variance along the angular direction, extracted from the diagonal values of the covariance matrix. The radius of the damage location was then determined by searching the maximal amplitude in the gradient orientation map along the radius line at the angle F_d obtained in the previous step. Furthermore, the column elements at each F_d could be extracted for damage

characterization revealed by the correlation between various damage patterns when multiple defects were present.

Results

Each defect type was placed independently at its corresponding location as indicated above, and the procedure was applied. Figs. 2-4 show the results for D1, D2, and D3, respectively. In all cases, the procedure gave unique, statistically unambiguous indications of the defect location. Each figure shows, from left to right, the gradient map, the covariance matrix, and the variance "slice" from the covariance matrix, all used to inform and highlight the defect location. While localization of the defect was very clear, characterization of the defect was more ambiguous; defects D1 and D2 were not in any way "directly imaged" by the gradient map approach, but interestingly, D3 (the delamination) was very clearly highlighted. The square Teflon insert in Fig. 4(c) is exactly indicative of the actual size. While this method was originally designed to localize and not characterize defects, clearly some aspect of the scattering—depending on the scatterer characteristics—directly affect the time-accumulated orientation gradient can directly encode some measure of scattered response, revealing geometric structure of the defect.
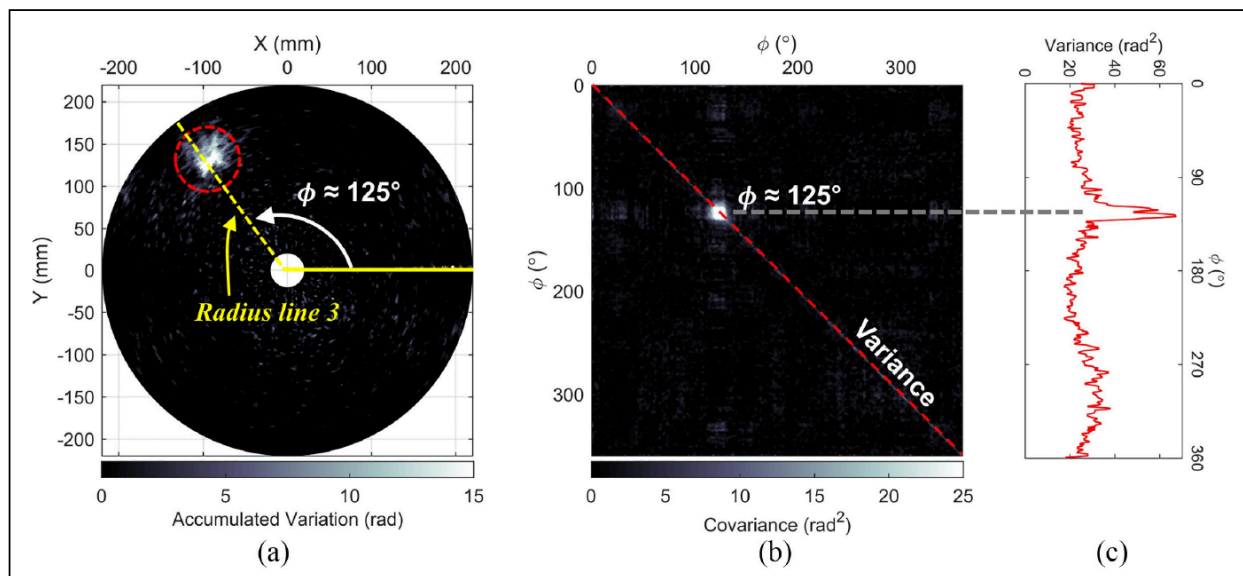

Fig. 2. (a) Accumulated gradient orientation map, (b) covariance matrix, and (c) variance subset for defect D1. Reproduced with permission from Ref. [13].
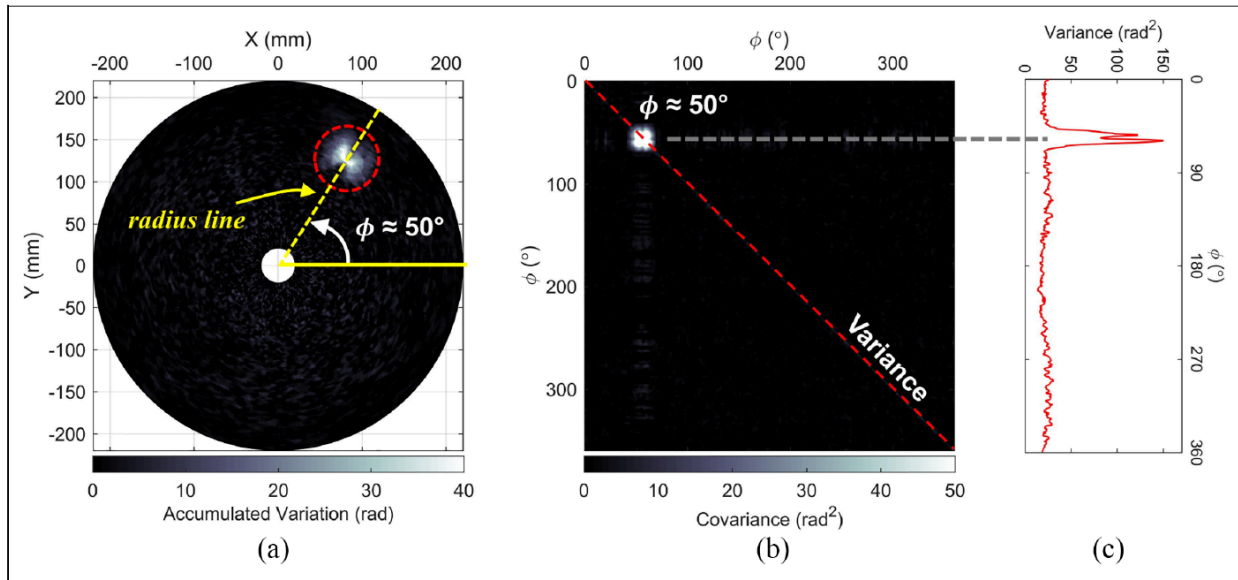
Fig. 3. (a) Accumulated gradient orientation map, (b) covariance matrix, and (c) variance subset
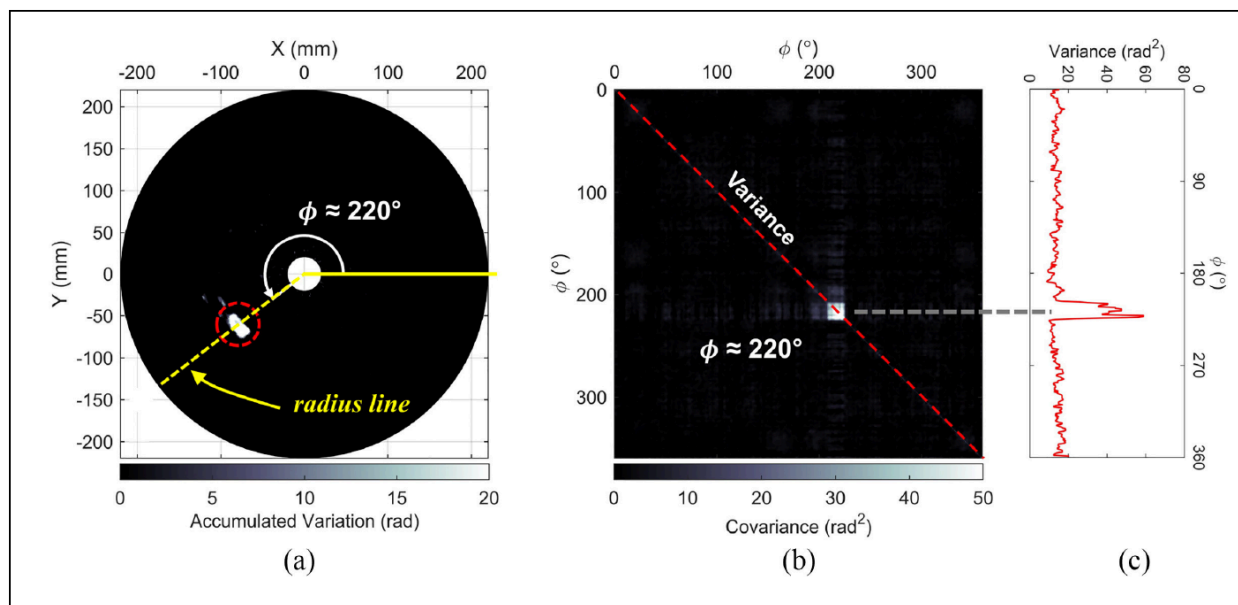for defect D2. Reproduced with permission from Ref. [13].

Fig. 4. (a) Accumulated gradient orientation map, (b) covariance matrix, and (c) variance subset
for defect D3. Reproduced with permission from Ref. [13].

Next, a simultaneous multi-defect test including all three scatterers D1, D2, and D3 located at
L1, L2, and L3, respectively, was conducted. Fig. 5 shows the same information as Figs. 2-4 for
this damage case. From the diagonal values of the covariance matrix in Fig. 5(b), the angular
directions of three defects were determined to be 50°, 125°, and 220° with radial locations 164 mm,
160 mm, and 132 mm, all of which were correct to within the spatial sampling of 1 mm. The
covariance map demonstrates that no correlation appears in the off-diagonal area, since the defects
share little scattering similarity.

As a final damage scenario test, three identical pieces of plasticine denoted D1 were placed at
locations L1, L2, and L4. The algorithm correctly located the three defects just as in the defect-

diverse previous test as Fig. 6 shows, but the correlation map reflects the similarity of the defects. The three concentrated amplitudes observed in the off-diagonal areas of the covariance map (high correlation) revealed that nominally identical defects would result in high covariance between their angles as well due to their similarity. This would make sense since the approach does, in some way, reflect unique scattering properties. This is a topic of further study.
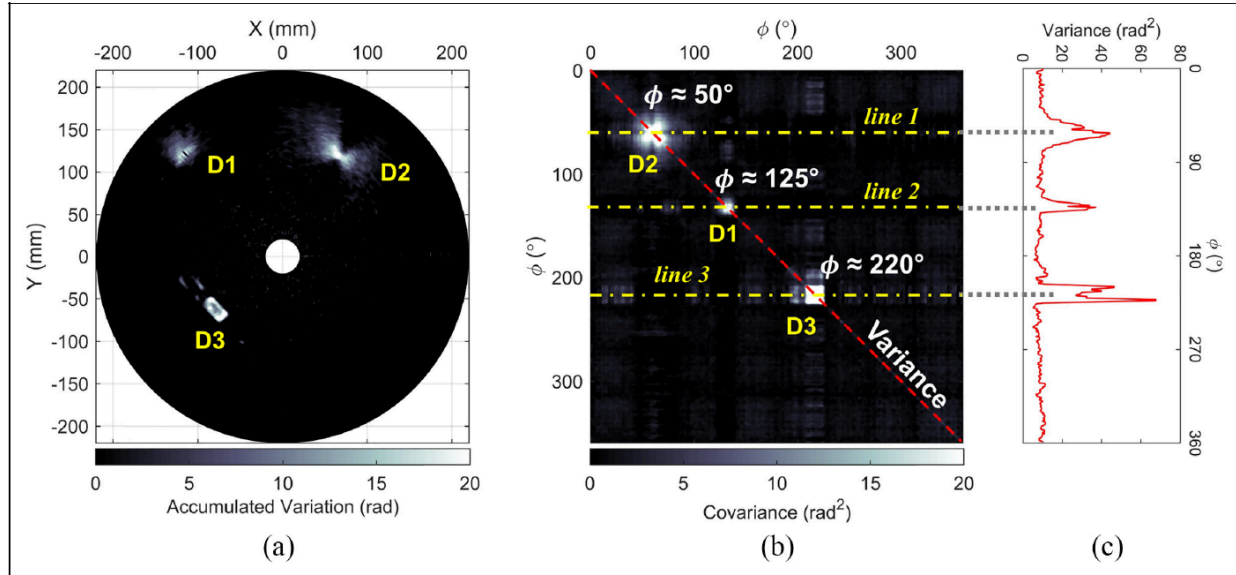

Fig. 5. (a) Accumulated gradient orientation map, (b) covariance matrix, and (c) variance subset for all different defects simultaneously. Reproduced with permission from Ref. [13].
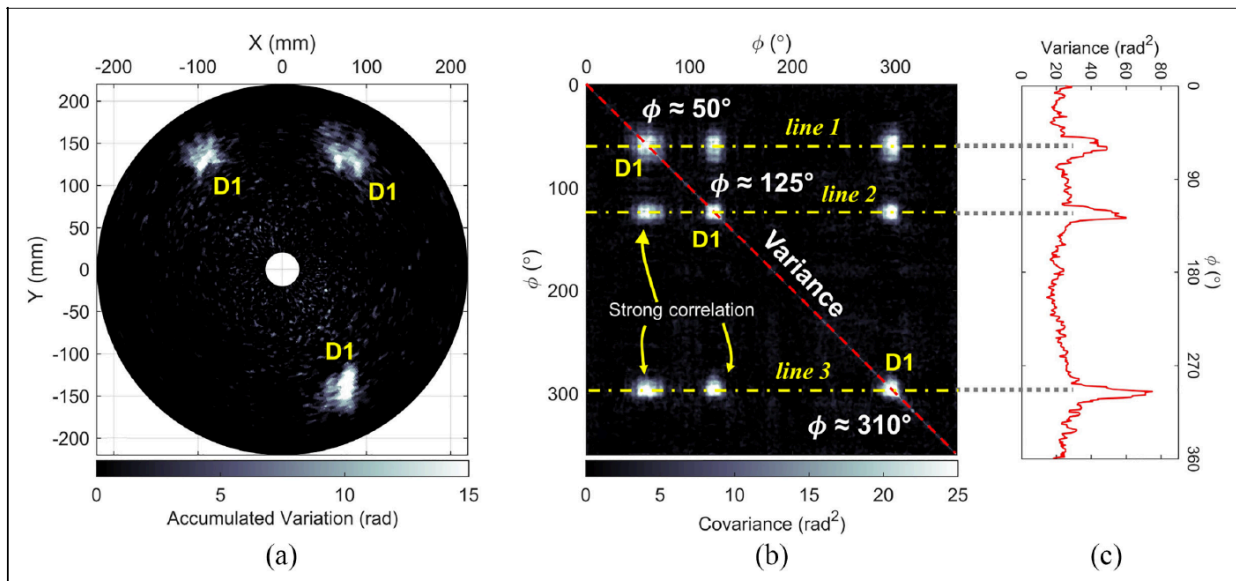

Fig. 6. (a) Accumulated gradient orientation map, (b) covariance matrix, and (c) variance subset for simultaneous placement of nominally identical defects. Reproduced with permission from Ref. [13].

Conclusions

Laser ultrasonic imaging of the wavefield spatial gradients was proposed for damage visualization and (primarily) localization in this work. The accumulated gradient orientation field or, combined with a covariance formation technique, revealed a distinctive localization of defects and in some cases provided clear imaging of the size. The proposed method was tested on a 3 mm aluminum

plate with both individual and simultaneous artificially introduced defects. The residual gradient orientation map showed the ability to detect these defects even under the impact of reflected waves. For the multiple simultaneous defect case, the covariance lines at each angle were extracted which indicated similarity (defect-to-defect correlation) among different types of defects. The approach consistently provided unique, correct localization, and depending upon the scatterer, it also provided clear imaging of the defect geometry itself. More work is needed to understand how accumulated gradient behavior can reflect consistent scattering patterns for the case of characterization.

References

[1] J. L. Rose, A vision of ultrasonic guided wave inspection potential, Proceedings of the 7th ASME NDE Tropical Conference-2001, San Antonio, USA (2001), 1-22.

[2] J. L. Rose, The upcoming revolution in ultrasonic guided waves, Nondestructive Characterization for Composite Materials, Aerospace Engineering, Civil Infrastructure, and Homeland Security 2011, Int. Society for Optics and Photonics vol. 7983 (2011), 798302. https://doi.org/10.1117/12.897025

[3] F. G. Yuan, Structural Health Monitoring (SHM) in Aerospace Structures, Woodhead, Cambridge, 2016.

[4] C. C. Chia, J. R. Lee, and C. Y. Park, Radome health management based on synthesized impact detection, laser ultrasonic spectral imaging, and wavelet-transformed ultrasonic propagation imaging methods, Composites Part B: Engineering 43(8) (2012) 2898–2906. https://doi.org/10.1016/j.compositesb.2012.07.033

[5] J. R. Lee et al., Laser ultrasonic propagation imaging method in the frequency domain based on wavelet transformation, Optics and Lasers in Engineering 49(1) (2011), 167–175. https://doi.org/10.1016/j.optlaseng.2010.07.008

[6] H. Sohn et al., Delamination detection in composites through guided wave field image processing Composites Science and Technology 71(9) (2011), 1250–1256. https://doi.org/10.1016/j.compscitech.2011.04.011

[7] Z. Tian and L. Yu, Lamb wave frequency–wavenumber analysis and decomposition, Journal of Intelligent Material Systems and Structures 25(9) (2014), 1107–1123. https://doi.org/10.1177/1045389X14521875

[8] H. Y. Chang and F. G. Yuan, Damage imaging in a stiffened curved composite sandwich panel with wavenumber index via Riesz transform, Structural Health Monitoring 19(3) (2020), 902–916. https://doi.org/10.1177/1475921719858432

[9] J. B. Harley and C. C. Chia, Statistical partial wavefield imaging using lamb wave signals, Structural Health Monitoring 17(4) (2018), 919–935. https://doi.org/10.1177/1475921717727160

[10] B. Park, H. Sohn, and P. Liu, Accelerated noncontact laser ultrasonic scanning for damage detection using combined binary search and compressed sensing, Mechanical Systems and Signal Processing 92 (2017), 315–333. https://doi.org/10.1016/j.ymssp.2017.01.035

[11] S. Y. Chong and M. D. Todd, Dispersion curve estimation via a spatial covariance method with ultrasonic wavefield imaging, Ultrasonics 89 (2018), 46–63. https://doi.org/10.1016/j.ultras.2018.04.012

[12] E. B. Flynn et al., Structural imaging through local wavenumber estimation of guided waves, NDT & E International 59 (2013), 1–10. https://doi.org/10.1016/j.ndteint.2013.04.003

[13] Z. Wu, S. Y. Chong, and M. D. Todd, Laser ultrasonic imaging of wavefield spatial gradients for damage detection, Structural Health Monitoring 20(3) (2021), 960-977. https://doi.org/10.1177/1475921720951336

[14] S. P. Liou and R. C. Jain, Motion detection in spatiotemporal space. Computer Vision, Graphics, and Image Processing 42(2) (1989), 227–250. https://doi.org/10.1016/0734-189X(89)90134-5